Comparison of 15Cr-15Ni austenitic steel cladding tubes obtained by HPTR cold pilgering or by cold drawing

L. Courtin, Stéphane Urvoy, Didier Bossu, Sophie Bosonnet, Michel Tabarant, Bouzid Kedjar, Patrick Olier, L. Thilly

Comparison of 15Cr-15Ni austenitic steel cladding tubes obtained by HPTR cold pilgering or by cold drawing

L. Courtin[1,a], S. Urvoy[1,b], D.Bossu[1,c], S. Bosonnet[1,d], M. Tabarant[2,e], B. Kedjar[3f], P. Olier[1,g,*], L. Thilly[3,h]

[1] CEA Saclay, DEN, DMN, SRMA – 91191 Gif-sur-Yvette France

[2] CEA Saclay, DEN, DPC, SEARS – 91191 Gif-sur-Yvette France

[3] Institut Pprime, CNRS-Université de Poitiers-ISAE ENSMA - France

[a]laurine.courtin@cea.fr, [c]didier.bossu@cea.fr, [d]sophie.bosonnet@cea.fr, [e]michel.tabarant@cea.fr, [f]bouzid.kedjar@univ-poitiers.fr, [g]patrick.olier@cea.fr, [h]ludovic.thilly@univ-poitiers.fr

Keywords: austenitic steels, 15Cr-15Ni, AIM1, cladding, HPTR cold pilgering, cold drawing

Abstract. Due to their high void swelling resistance, work-hardened titanium stabilized austenitic steels have been chosen as cladding material for sodium cooled fast reactor. In this study, HPTR cold pilgering process is compared to cold drawing at the last shaping step of the tube processing. The effects of the cold work accumulation and heat treatments are studied in connection with the microstructure (grain size), the hardness and the texture. The following results were found:
- As larger amount of cold work can be applied by HPTR cold pilgering, a lower number of intermediate heat treatments are required. In addition, the bending of the tube is significantly reduced after each pass for this process allowing for a limitation of the straightening operations.
- For both processes, optical micrographs show micrometric titanium carbide precipitates and the presence of deformation twins on a few grains on the final tube. A significant grain size refinement from ≈45 μm to ≈17 μm can be obtained by reducing annealing temperature from 1403K down to 1353K. For the latter, the precipitated mass fraction measured by selective dissolution of the alloy matrix is the largest, revealing a possible negative impact on swelling under irradiation.
- Through-wall Vickers hardness profiles show an increase of the hardness at the outer diameter for HPTR cold pilgering whereas the hardness profile remains continuous for cold drawing. It is found that the Q-factor has an influence on these wall-thickness hardness profiles.
- For each process, neutron diffraction measurements on finished tubes reveal two main fiber texture components ⟨111⟩ and ⟨100⟩ parallel to the tube axis with differences in their relative intensities.

Introduction

Sodium Fast Reactors (SFRs) have been selected as the reference type in France, leading to extended studies dedicated to the ASTRID reactor (Advanced Sodium Technological Reactor for Industrial Demonstration) to be built in the next decade [1,2]. For the first core of Astrid, the cladding tubes of the fuel assembly will be fabricated with the grade reference, so-called 15/15Ti AIM1 (Austenitic Improved Material #1) [2], experienced in the past in the former french sodium reactors.

The void swelling resistance of this alloy has been improved by optimizing the minor element amount (Ti, Si, P, B), and addition of swelling inhibitors (Ni) [3, 4, 5]. This material is used after a prior cold work (CW) of about 20-25% resulting in defects such as dislocations which interact with point defects produced by neutron irradiation thus enhancing recombination and hence making this alloy more resistant to irradiation swelling [5]. The cold-worked level and the stabilization by Ti allow for delaying the beginning of the swelling under irradiation and make AIM1 suitable for use up to 110 dpa at least which is the required target for Astrid first core [6, 7].

Ingots of AIM1 steel are usually made by primary vacuum induction melting process (VIM) followed by a secondary melting performed by vacuum arc remelting (VAR). After prolonged soaking at ~1200°C to homogenize the cast ingots, they are hot forged to obtain bars. These bars are hot extruded and then machined including drilling operation in order to obtain hollow round primary shape. The cold drawing steps allow for getting the final cladding from the hollow round primary shape. The heat treatment conditions are optimized to achieve the best microstructure (grain size) in relation with the suitable level of tensile properties.
In this paper the attention is specifically focused on the final cold working stage. The cold drawing process is the reference used in the past to achieve the cladding tubes for example for French SFRs like Phenix or SuperPhenix. But an alternative process such as the cold pilgering (which has widely proved satisfactory results in the field of zirconium-based cladding tube for WPR reactor) can be envisaged too. In addition, this process is also investigated for ODS-steel cladding [8,9].
This study gives a comparison of characteristics obtained on cladding tubes manufactured at laboratory scale level processing either by cold drawing or by HPTR cold pilgering, including appropriate heat treatments. The impact on the grain size, precipitates, hardness and texture is investigated.

Material – Fabrication route

Material

Chemical composition is determined on extruded bar by several techniques chosen as a function of the analyzed element: Optical Emission Spectroscopy (OES), Combustion and Infrared Absorption (CIA) and Plasma Emission Spectrometry (PES). The chemical composition is reported in Table I.

Table 1: Elemental composition range of AIM1 (in wt. %)

	Cr	**Ni**	**C**	**Mo**	**Mn**	**Si**	**P**	**Ti**	**S**
Weight%	14.0	15.6	0.091	1.52	1.65	0.85	0.041	0.40	0.003
Uncertainty	±0.25	±0.20	±0.03	±0.03	±0.03	±0.02	±0.003	±0.01	±0.001
Method	*OES*	*PES*	*CIR*	*OES*	*OES*	*OES*	*OES*	*OES*	*CIR*

Fabrication route

The figure 1 presents the two different fabrication routes used for manufacturing cladding tubes. From an extruded bar, a rod of 20 mm diameter is obtained by cold swaging. This rod is drilled and then mother tubes are processed either by HPTR cold pilgering or by cold drawing.
Cold processing requires in each case several passes and intermediate heat treatments. Finally, the tubes are subjected to a solution annealing at 1353K or 1453K for 2 minutes before the last pass of cold working which leads to a CW of $\varepsilon \approx 18\%$ or 23% (*with* $\varepsilon = \Delta S/S_0$, *S is the section of the tube*).
By comparing the cold processing stages, it can be pointed out that HPTR cold pilgering offers certain technological benefits:
- The bending of the tube is significantly reduced after each pass for this process allowing a limitation of the straightening operations.
- A heat treatment is performed after each pass for cold drawing in order to protect the durability of the drawing tools (dies and mandrels). In contrast, a larger amount of cold work can be applied by HPTR cold pilgering (several cumulated passes) coupled with a lower number of intermediate heat treatments.
- A drawing tag is required for cold drawing which leads to a wasting of material at one extremity of the tube.

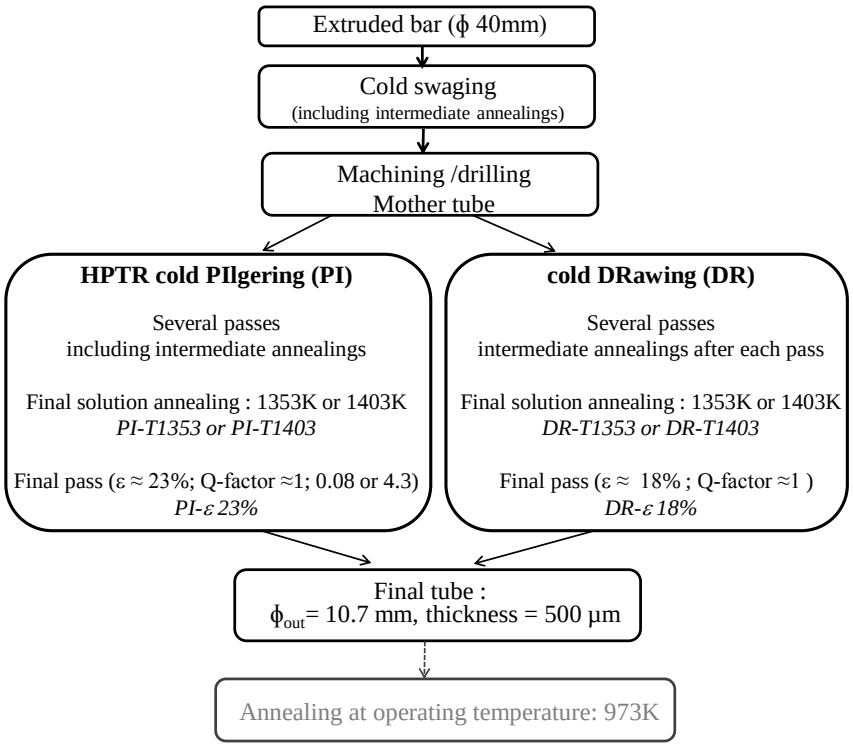

Figure 1: Fabrication route used for cladding tubes manufacturing

Experimental

Optical microscopy with motorized stage is carried out on transverse cross-section with a Reichert MeF-3. The samples are observed after standard metallographic preparation and electrolytical etching with 60% nitric acid. Grain size measurements are performed by using image analysis (Visilog software). Several thousand of grains are analyzed in each case.

Selective dissolution of the matrix is carried out by electrochemical method. This method allows for recovering a residue comprising a selectively extracted phase. This residue can be analyzed and the precipitated mass fraction can be determined. For the dissolution to be quantitative dissolved mass is 20g minimum. The electrolyte used is composed with 10% of hydrochloric acid and 90% of methanol. Dissolution is carried out with a constant intensity (1 ampere).

Wall thickness hardness profiles are realized on transverse cross-sections by using:

- Micro-hardness measurements performed with a VMHT30a - LEICA tester with a test force of 100 grams,
- Berkovich measurements carried out with a nanoindenter NHT^2 - CSM with a 250 mN load. Every measurement is performed with a minimum spacing of about 20-30µm width (around 2.5 footprint) between each hardness point. The following equation allows the conversion of Berkovich values in Vickers.

$$HV_{IT} = \frac{H_{IT} \times A_P}{g_n \times A_s} = 0{,}0926\ H_{IT} \quad (1)$$

with: g_n the acceleration of gravity, A_p the projected contract area of penetrator , A_s the surface area of the penetrator, H_{IT} the indentation or penetration Berkovich hardness and HV_{IT} the indentation or penetration Vickers hardness.

Crystallographic textures are measured by neutron diffraction using a 4-circle diffractometer (6T1) at Leon Brillouin Laboratory (LLB) Orphée (CEA Saclay-CNRS). Diffraction experiments are performed in transmission mode with wavelength λ= 0.1159 nm. The analyzed volume is about a few cm^3. Pole figures are measured for (111) (200) and (220) planes. The Labotex software is used for computing the results.

Results

Optical microscopy - Grain size

The figure 2 shows optical micrographs obtained on cladding tube's transversal cross section either for cold drawing or for HPTR cold pilgering, respectively.

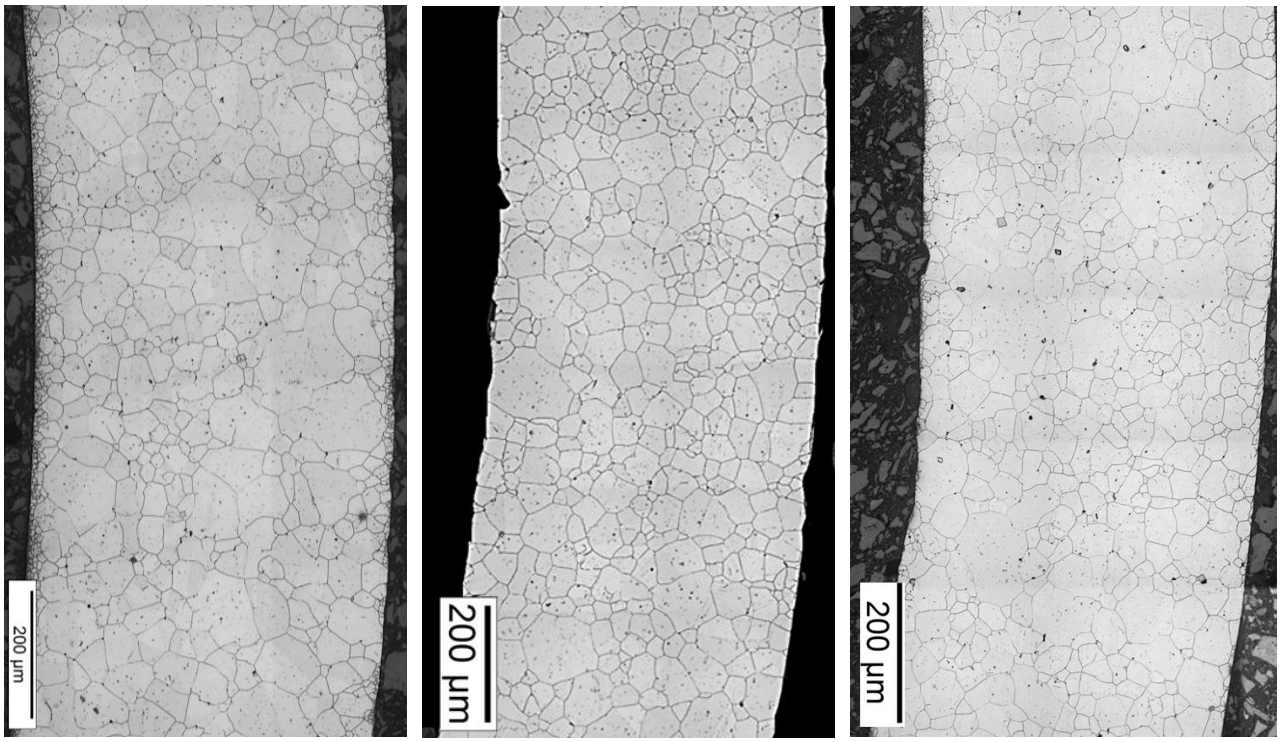

a) DR-T1403 (ϕ_{moy} = 45± 29µm)

b) PI-T1403 (ϕ_{moy} = 58± 19µm)

c) DR-ε 18 (ϕ_{moy} =42± 24µm)

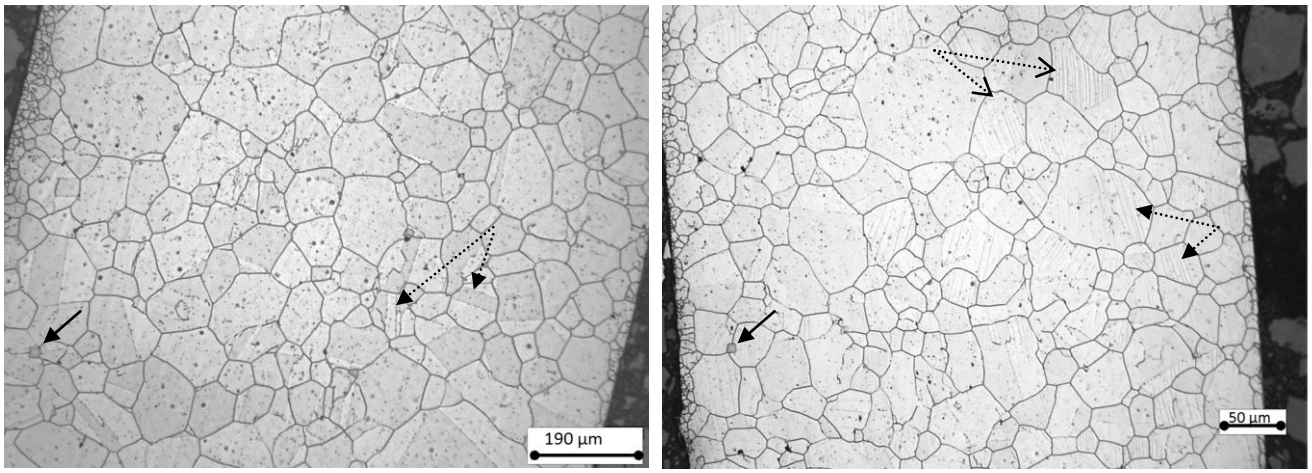

d) DR-T1403

e) DR-ε 18

Figure 2: Optical micrographs showing grain size : a and d) after cold drawing and last solution annealing at 1403K, b) after HPTR cold pilgering and last solution annealing at 1403K c and e) after solution annealing at 1403K followed by 18% of CW (drawing)

For both processes, the optical micrographs show the presence of micrometric titanium-based carbide precipitates (*solid black arrows in figure 2d, e*) identified by EDS analysis. The largest (a few µm up to 20µm) precipitates appear as square inclusions (primary precipitate) while the black dots correspond to a population of finest (a few hundred on nanometers) TiC secondary carbides.

Some thermal twins are revealed on a few grains on annealed material (*dotted black arrows on Fig. 2d*) whereas some mechanical twins are observed only after CW on a few grains (*dotted black arrows on Fig. 2e*).
It can be seen that there is not a large grain size difference on tubes before last pass (after last heat treatment) for each process (about ≈ 45 µm for cold drawing and ≈ 58 µm for HPTR pilgering after SA, respectively). This size is slightly decreased after 18% of CW (ϕ_{moy} ≈ 42 µm for cold drawing). However, by reducing the temperature of the last solution annealing a significant grain size refinement can be obtained. The grain size is decreased more than twice by reducing of about 50K the temperature of this last heat treatment (1353K instead of 1403K) as shown on the Fig. 3. In this case, the mean grain size diameter is about ≈ 16 µm for HPTR cold rolling and ≈ 17 µm for cold drawing, respectively.

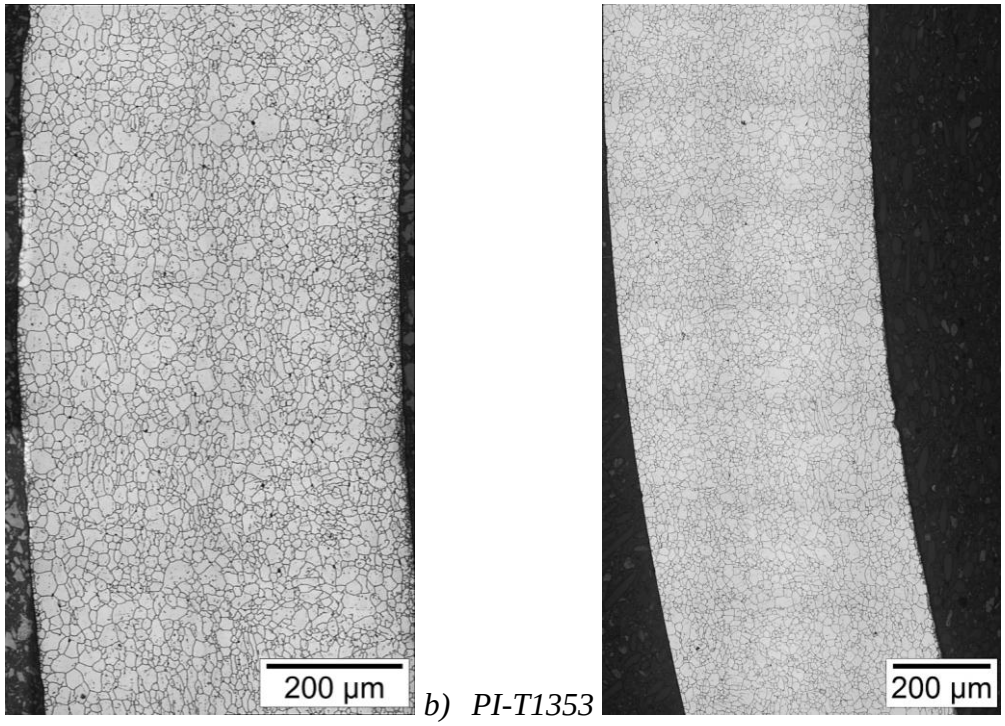

a) DR-T1353 (ϕ_{moy} =16± 9µm) *b) PI-T1353 (ϕ_{moy} = 17± 8µm)*

Figure 3: Optical micrographs showing grain size: a) after cold drawing and last solution annealing at 1353K, (b) after HPTR cold pilgering and last solution annealing at 1353K

Since the last solution annealing can modify the titanium carbides dissolution, a quantification of the precipitates and the determination of the titanium content in solid solution are performed by using selective dissolution.

Precipitate fraction
The weight ratio of precipitate is measured by using selective electrochemical dissolution of the alloy matrix. These measurements are carried out on the mother cold swaged bar for two different heat treatment temperatures i.e. 1353K or 1403K. For the case of a temperature of1403K), two selective dissolutions were performed in order to establish a reproducible experimental procedure, leading to a precision of the fraction of precipitates of 0.02%.
The weighing of the previously dried filter before and after extraction makes it possible to deduce the total mass fraction from recovered precipitates. In addition, by chemically analyzing the liquid solution and the residue it is possible to obtain the titanium fraction in solid solution and the content of the main metallic elements which are present in the residue. The results are reported on Table 2.

Table 2: Precipitates and titanium fraction measured after selective dissolution and chemical analysis of the residue.

	Batch 1 (1353K)	Batch 2 (1403K)	Batch 3 (1403K)
Mass fraction of precipitate (wgt %)	0.483	0.402	0.395
Titanium fraction in solid solution (wgt %)	0.41	0.57	0.55
Chemical analysis (wgt%) (main metallic elements) *	Ti: 67.8 ; Mo: 4.0 Cr: 16.8 ; Fe: 4.6	-	Ti: 68.4 ; Mo: 3.6 Cr: 12.2 ; Fe: 5.1

**average values obtained from the ICP-MS analysis of 6 samples for each residue*

The total mass fraction of precipitates measured is reproducible for the same treatment temperature (1403K) with a percentage of about 0.40%. At lower temperature (1353K), the mass fraction is larger around 0.48%; indicating that their redissolution in solid solution is less efficient.
By referring to results obtained on cladding in AIM1-precursor irradiated in Phenix [10], it can be expected that the lower temperature (1353K) leads indeed to a detrimental effect on irradiation swelling.
The titanium fraction in solid solution is inversely proportional to the mass fraction of precipitate. At 1403K, the percentage is in the range 0.55-0.57% and at a lower temperature (1353K) this fraction is only around 0.41%. It is correlated with the fact that titanium is the main element present in these precipitates (TiC or (Ti,Mo)C primary/secondary carbides [10]) as shown in table 2 (Ti ~ 68% in wgt). For the both temperatures, the contents in titanium, molybdenum and iron are very close. Only the chromium content is found higher at 1353K (16.8%) compared to 1403K (12.2%). One can suggest that it can be related to the presence of a small amount of chromium carbides which should remain undissolved at 1353K.

Hardness profiles – Q factor effect
Through-wall Vickers hardness profiles are measured at different stages of the fabrication route for HPTR cold pilgering and for cold drawing (Fig. 4).

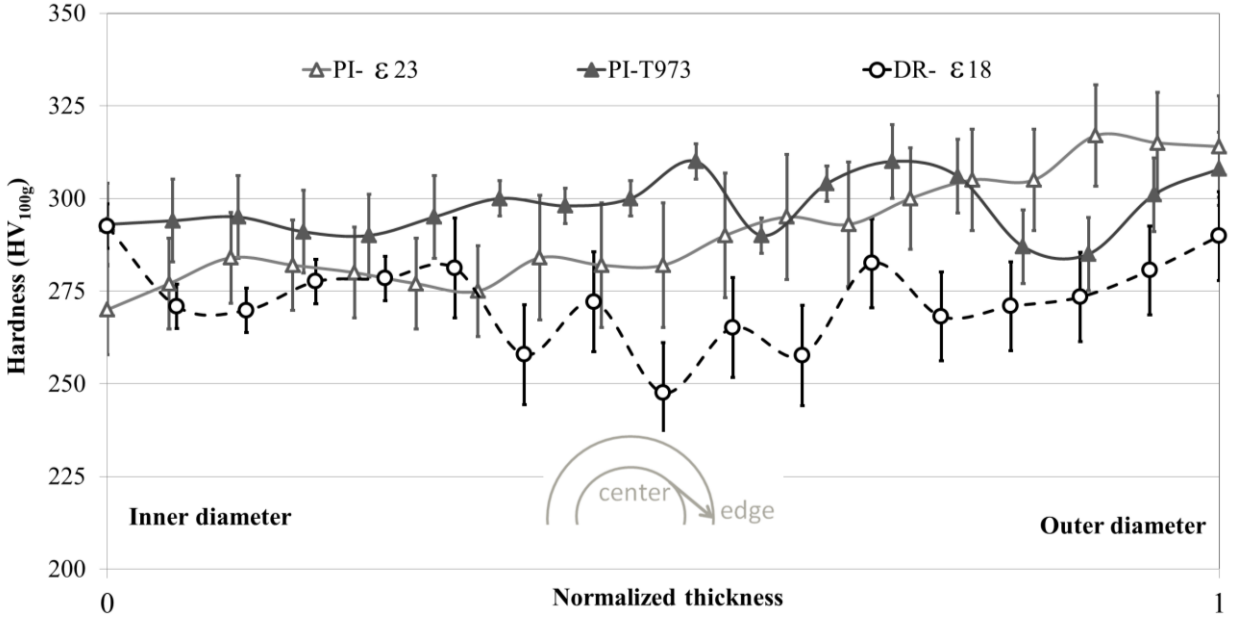

Figure 4: Hardness evolution across wall thickness on cladding tubes processed by cold drawing (ε≈18%) or by HPTR cold pilgering in CW condition (ε≈23%) or after annealing at 973K

Figure 4 shows that the hardness values are in the range 250-350 HV for all the samples. In CW condition, the mean hardness value are slightly lower for cold drawing compared to HPTR pilgering which can be related to the lower degree of CW (18% instead of 23%). Hardness profiles reveal a

gradual rise in micro-hardness from 270-280 HV on the inner diameter side to about 300-320 HV on the outer diameter side for HPTR cold pilgering whereas the hardness profiles remain flat or constant for cold drawing. The hardness gradient is strongly reduced for HPTR pilgering after a heat treatment at operating temperature (973K, 4h.)

Previous studies have pointed out that the hardness gradient in austenitic steels tubes obtained by cold drawing should be linked to the Q-factor [11]. Indeed, different applied strain path determine different relative changes in the diameter and wall thickness of the tube. The relationship between the relative variation of the wall thickness and the tube outer diameter is known as strain-ratio factor or Q-factor:

$$Q = \frac{(E-e)/E}{(D-d)/D} \quad (2)$$

Where E, D and e, d are the thickness and the outer diameter before and after the rolling pass, respectively.

For the current fabrication, a Q-factor value close to 1 has been selected for the last pass of cold drawing. But, for HPTR cold pilgering, three values of Q-factor are tested: 0.08; 1.0; 4.3. Three tubes were obtained and for each of them a transversal cross section was subjected to nanoindendation profiles on 12 generating lines tilted by 30° each.

The mean hardness profiles obtained for each Q-factor are reported on the figure 5.

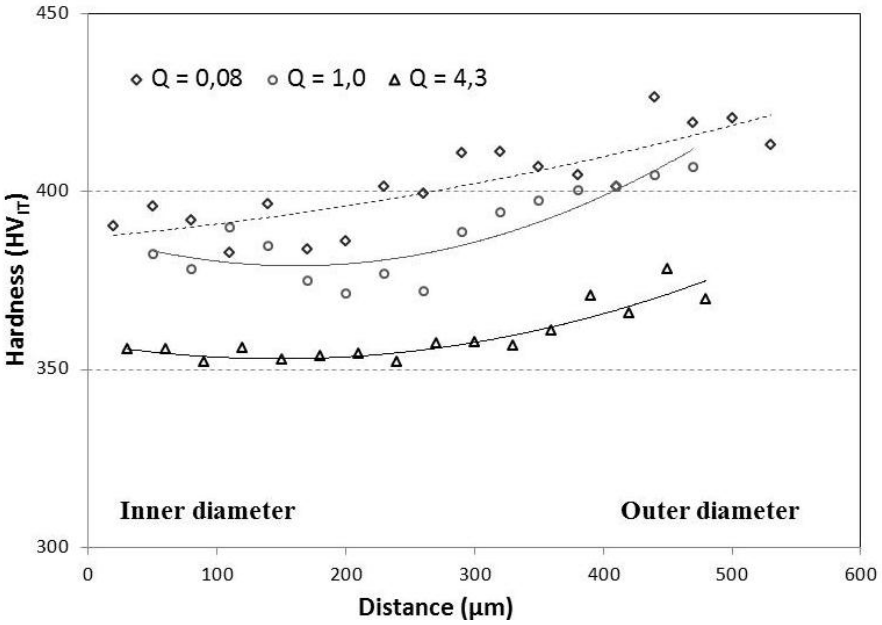

Figure 5: Hardness evolution across wall-thickness for with different Q-factor

It is indeed verified that for the same cold work level (ε ≈ 23%), the higher the Q-factor value, the lower the mean hardness value measured across the wall-thickness. The same trend is observed for 304L stainless steel deformed by cold drawing [11]. In addition, it seems that the hardness values are more heterogeneous for a pass with a low Q-factor value: for Q=0.08, no inflection of the trend curve is observed across the wall-thickness. It should be interesting to check if the tensile properties of the cladding are also influenced by the applied Q-factor.

Texture measurements

Each cold working process is expected to lead to a specific crystallographic texture which needs to be analyzed in view to understand the deformation mechanism and to have a better control of the fabrication. Figure 6 presents Pole Figures (PFs) calculated from experimental data with LaboteX software. The three upper calculated PFs provide information on texture components of the final tube obtained from drawing process and the three other calculated PFs below correspond to the final tube obtained from HPTR pilgering process.

In both samples, high intensity at centers of ⟨111⟩ and ⟨200⟩ PFs can be observed which suggests two texture components, ⟨111⟩ and ⟨200⟩, in the tube axis direction, DA (Table 3). Moreover, the presence of regular intensity rings at specific χ angles advocates for fiber textures. This is confirmed by the perfect matching between the experimental rings and theoretical ones calculated in the case of perfect fiber components and added to the experimental PFs.

If the two samples exhibit similar fiber texture components (⟨111⟩ and ⟨200⟩), their respective strength is different as shown by the intensity values presented in table 3: this may be reasonably attributed to the different thermo-mechanical treatments undergone by the two types of tubes. As shown by literature data, it is typical to obtain a strong ⟨111⟩ texture in severely cold drawn FCC metals while the ⟨100⟩ texture is generally attributed to (dynamic) recrystallization [12].

The fact that the present study results from a deep volume analysis (neutron diffraction with penetration of several centimeters) does actually question on the spatial distribution of the two texture components, i.e. whether they are homogeneously distributed or located in different regions of the tubes (e.g. external or internal sub-surface of the tubes). Is it expected that laboratory x-ray diffraction will bring some elements of answer due to the lower penetration depth of X-radiation.

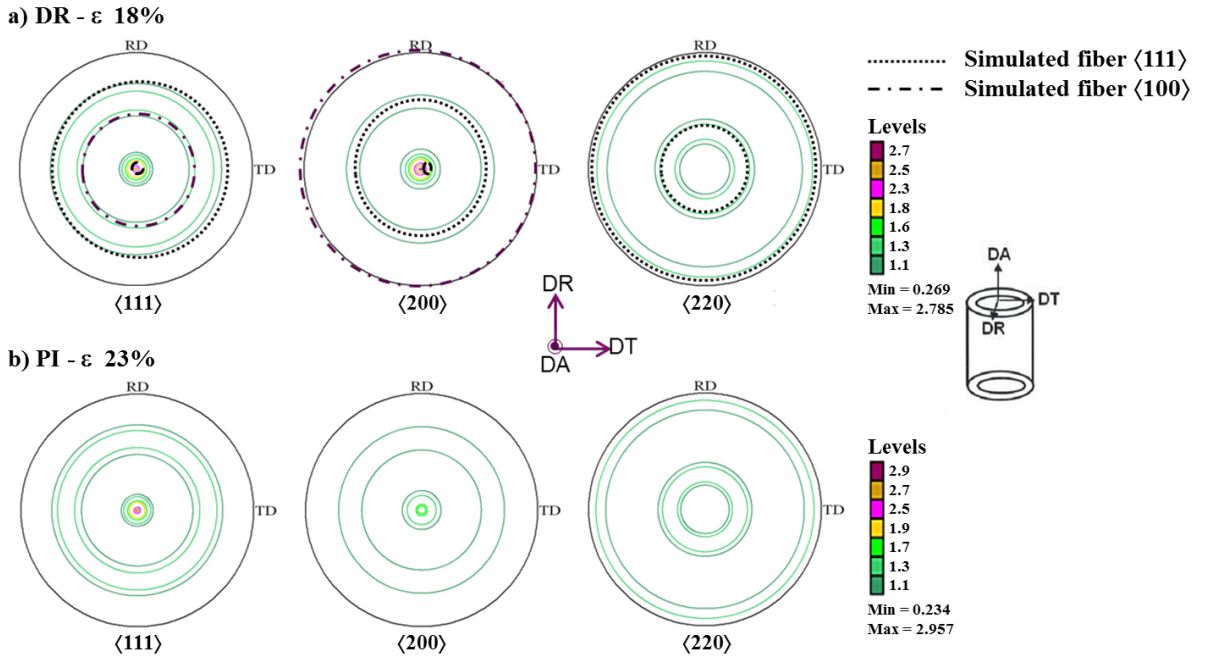

Figure 6 : Calculated Pole Figures obtained by neutron diffraction on final tubes (axial section) a) cold drawing b) HPTR cold pilgering (DA is the rolling direction)

Table 3. Maximal intensities measured on pole figures by neutron diffraction for each cold process

	⟨111⟩	⟨200⟩	⟨220⟩
Cold drawing (DR-ε18)	3,0	3,3	1,9
HPTR cold pilgering (PI-ε23)	3,5	2,5	1,9

Conclusion

In this study, HPTR cold pilgering process was compared to cold drawing at the last shaping step of the tube processing. The effects of the cold work accumulation and heat treatments were studied in connection with the microstructure (grain size), the hardness and the texture. The main results are the following:

- It seems that the use of each cold working process does not result in large differences on grain size and texture. The grain size is mainly dependent of the solution annealing temperature applied just before the final cold working step.
- The average level of hardness is not changed by the cold working process for equivalent accumulated strain. But it seems that there is a larger gradient in micro-hardness from inner diameter side to outer diameter side in the case of HPTR cold pilgering with higher hardness values near the outer diameter. This hardness heterogeneity is drastically reduced after a thermal ageing of 4 hours at a temperature of 973K.
- It is demonstrated that for the same cold work state, the higher the Q-factor value, the lower the mean hardness value across the wall-thickness.
- By analyzing the texture of final tubes obtained by cold drawing or by HPTR cold pilgering, two main fiber textures were found ⟨111⟩ and ⟨200⟩ parallel to the rolling direction, as expected in FCC metals after processing involving cold working and annealing steps.

Acknowledgements:
The authors are grateful to M.H. Mathon (LLB Orphée- CEA Saclay) for experimental neutron diffraction measurements.

References

[1] M. Le Flem, P. Gavoille, A. Courcelle, P. Olier, Y. De Carlan, "Status of the French R&D on Astrid core Materials" Proc. of ICCAP 2014, Charlotte, USA, (2014) paper 14117.

[2] M.S. Chenaud and al., "Status of the ASTRID core at the end of the pre-conceptual design phase 1" Nuclear Engineering and Technology Special Issue, vol. 45, 6 (2013).

[3] P. Dubuisson, V. Levy, J.L. Seran "Austenitic stainless steel particularly usable as a core structural or canning material in nuclear reactor", US patent N° 4,778,651 (1998).

[4] E.H. Lee, L.K. Mansur, J. Nucl.Mater., 278 (2000), 11-19.

[5] M. Le Flem, M. Blat-Yrieix, V. Garat and J.L. Séran, "French R&D on materials for the core components of Sodium Fast Reactor", Proc. of the *Int. Conf. on Fast Reactors and Related Fuel Cycles: Safe Technologies and Sustainable Scenarios (FR13)*, Paris, France (2013).

[6] J.L. Séran and al., "Behavior under neutron irradiation of the 15-15Ti and EM10 steels used as standard materials of the Phenix fuel subassembly," Proc. of *Effects of Radiation on Materials: 15th International Symposium*, Nashville, Tenessee, USA (1992) 1209-1233.

[7] A. Maillard, H. Touron, J.M. Séran, A. Chalony, "Swelling and Irradiation Creep of Neutron-Irradiated 316Ti and 15-15Ti Steels," Proc. of *Effects of Radiation on Materials: 16th International Symposium*, Aurora, Colorado, USA (1994) 824-837.

[8] L. Toualbi, C. Cayron, P. Olier, J. Malaplate, M. Praud, M.-H. Mathon, D. Bossu, E. Rouesne, A. Montani, R. Logé, Y. de Carlan, "Assessment of a new fabrication route for Fe–9Cr–1W ODS cladding tubes", Journal of Nuclear Materials, vol. 428, 47-53 (2012).

[9] L. Toualbi, P. Olier, E. Rouesne, D. Bossu,d, Y. De Carlan, « On the influence of cold rolling parameters for 14CrW-ODS ferritic steel claddings", Key Engineering Materials Vols. 554-557 (2013) pp 118-126

[10] JL Seran & al, patent CEA FR 2790089-A1, 1999.

[11] D. Vuillaume, P. Gerard, 23eme journée des aciers spéciaux de l'école des Mines de Saint-Etienne (communication in french), may 1984

[12] Kocks UF, Tome CN, Wenk HR. Texture and Anisotropy, Cambridge University Press; 2000. Hughes DA, Hansen N. Acta Materialia 1997; 45(9):3871.